Theory of negative-ion conversion of neutral atoms in grazing scattering from alkali halide surfaces

A. G. Borisov and V. Sidis
Laboratoire des Collisions Atomiques et Moléculaires (Unité associée au CNRS, URA 281), Bâtiment 351, Université Paris-Sud, F-91405 Orsay Cedex, France
(Received 17 March 1997)

The theoretical approach proposed by Borisov *et al.* [Phys. Rev. Lett. **77**, 1893 (1996)] to treat negative-ion conversion of neutral atoms at ionic crystal surfaces is described in detail. Due to the localization of the valence-band electrons at the anionic sites of the crystal, the conversion process is viewed as a result of successive binary collisions between the projectile and the negatively charged sites at the surface. Parameter-free calculations of F^- formation in grazing scattering from LiF(100) and KI(100) are performed using a model in which all sites of the crystal lattice but one, the active site, are represented by eventually polarizable point charges. Parallel velocity thresholds for negative-ion formation, relative efficiency of the negative-ion formation for LiF and KI crystals, and dependences of this efficiency on the scattering angle correspond well to the experimental results. [S0163-1829(97)08635-9]

I. INTRODUCTION

Charged particle-surface interactions have been a subject of intensive research over the past decades. Considering insulating surfaces of ionic compounds the most thorough studies have mainly focused on electron- and ion-stimulated desorption and sputtering[1–5] and on ion-induced electron emission.[6,7] The evolution of the charge state of the projectile during its interaction with ionic crystal surfaces has received attention only recently.[8–16] In experiments on the grazing scattering of positively charged and neutral H, O, F projectiles from alkali-halide surfaces very high fractions of negative ions were unexpectedly observed in the scattered beams.[9,13,15]

Until now the concepts for electron transfer from a surface to an atom essentially descend from atom/metal surface interaction studies.[17,18] In this case, the formation of negative ions is qualitatively well understood. Basically, when a neutral projectile approaches a metal surface its affinity level is shifted down due to the *image potential*. At small projectile-surface separations the affinity level is thus brought into resonance with occupied electronic states of the metal below the Fermi level. It can thereby be populated via *resonant electron capture* from the metal. As soon as the projectile moves away from the surface the populated level rises in energy and, at large atom-surface separations, it can be brought in resonance with unoccupied electronic states of the metal above the Fermi level. An electron transfer from the negative ion back to the metal becomes possible and may lead to the neutralization of the ion. These processes are presented schematically in Fig. 1(a). The final negative-ion population after the collision process is determined by the probability of the negative-ion formation by the electron capture close to the surface and its survival against electron loss when moving away from the surface. The rates of the electron loss/capture depend on the coupling between the electronic states of the negative ion and metal and can be calculated nowadays nonperturbatively.[19,20] In the case of grazing scattering, the parallel velocity may also help to bridge the gap between the Fermi level and the affinity level of the negative ion. This leads to the so-called *kinematically assisted negative-ion formation*.[17,18,21–23]

It follows from the preceding discussion that the basic electron transfer mechanisms for metal surfaces depend crucially on the position of the affinity level of the atom relative to the Fermi level of the solid. Based on these mechanisms, the finding of very high fractions of negative ions in grazing

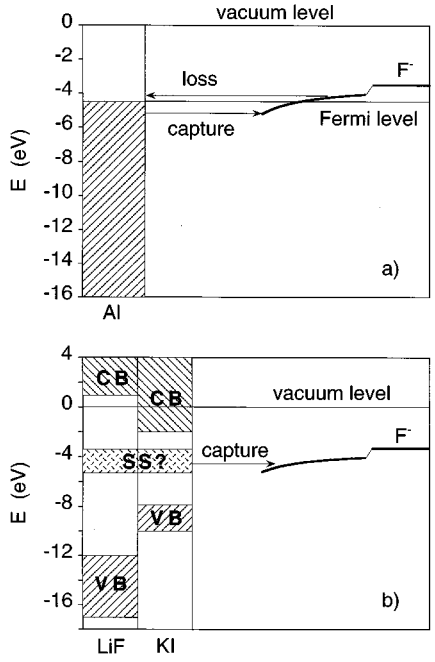

FIG. 1. Energy-level diagram for a F^- ion in front of a metal (Al) surface [part (a) of the figure] and in front of insulating LiF(100) and KI(100) surfaces [part (b) of the figure]. VB and CB stand, respectively, for the valence and conduction bands of the ionic crystal. SS indicates the position of surface states conjectured in Ref. 15 to invoke a resonant electron-capture mechanism.

scattering of F, O, H atoms on alkali-halide surfaces appeared at first sight very surprising. Indeed, alkali-halide surfaces are characterized by a *broad band gap*. Taking, for example, a LiF crystal [Fig. 1(b)], this gap extends from the binding energies of the valence-band electrons ($|E_v| > 12$ eV) to vacuum energies.[24,25] Moreover, image potential effects for a moving charge in front of an alkali-halide surface can be estimated not to exceed 1–2 eV.[26] Hence, over a broad energy range no electrons of the solid would be available for resonant electronic transitions to the affinity level of the atom. Consequently, one could conclude that negative-ion formation is hardly possible in this case which is in contradiction with the experiments.

It has been suggested[15,27] that the observed high negative-ion fractions could result from resonant electron capture from *occupied alkali-halide surface states*. The existence of such states in the right energy range and with a sufficient density had thus to be postulated. This explanation is actually at variance with experiments on Na^+ neutralization at alkali-halide surfaces. Indeed if the conjectured states existed the neutralization efficiency of Na^+ should have been comparable with F^- formation from F in similar conditions. This is so because the recombination energies of Na^+ in its ground state (5.139 eV) and first excited state (3.037 eV) are comparable with the electron affinity of F (3.45 eV). In addition, the energy difference between the F^- affinity level and the Na ground state level is attenuated close to the surface due to the image potential effect: the ground-state level of Na experiences an upward shift close to the surface while the F^- level moves downwards. Actually, the experimental data[28] show that positively charged alkali ions are not neutralized at alkali-halide surfaces in the low velocity regime where F^- ions were found to be efficiently produced from F. In fact, the experiments of Ref. 28 show that not only the density of occupied surface states but also that of the unoccupied ones is negligible in the few eV energy range. Additional information comes from the observation that Auger neutralization is suppressed in the scattering of noble gas ions from alkali-halide surfaces.[14] The latter phenomenon can be well understood as being due to the large band gap of ionic crystals; it would not exist in the case of an important population of the surface states conjectured in Refs. 15, 27. Finally, let us also mention that no evidence of such states was found in metastable helium atom deexcitation spectroscopy.[11]

The absence of occupied surface states in the few eV energy range has led us to propose a mechanism which could *shift the energy level* of the negative ion *and bring it to near resonance* with the valence band of the crystal for the duration of the atom-surface interaction. Our approach takes into account specifics of the electronic structure of ionic crystals, namely: the localization of the valence-band electrons at anionic sites. It considers the build up of the negative-ion fraction in the scattered beam as a result of *successive binary collisions with negative halogen sites at the surface*.[9,29] The present paper describes the details of this approach. It is organized as follows. Section II presents the basic mechanism which governs the electron transfer process. Section III describes the actual calculations: Sec. III A introduces the successive binary collision approach characterizing the model, Sec. III B is devoted to the treatment of the charge-transfer process in one binary collision, Sec. III C determines the inputs to the model using adaptations of quantum chemistry techniques, finally, Sec. III D copes with the problem of the trajectory. The results are presented and discussed in Sec. IV.

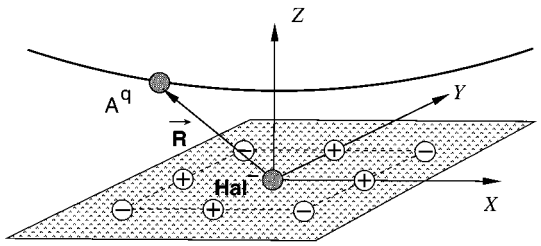

FIG. 2. Sketch of the binary interaction model for an A^q atomic projectile scattering from an ionic crystal. The shaded plane represents the portion of the ionic surface surrounding the active Hal^- site (dark central circle). The bold curve indicates the trajectory of the impinging A^q projectile (dark upper circle). The vector **R** locates the A^q projectile relative to the Hal^- active site taken as the origin of the coordinates.

II. THE BASIC APPROACH

The proposed electron-transfer mechanism is based on the property of the considered ionic crystals (LiF, KI) to have alternating $+1$ and -1 charge distributions at the lattice sites: Alk^+ (alkali) and Hal^- (halogen), respectively. The valence electrons are localized at the Hal^- sites and the valence band of alkali-halide crystals is formed from the Hal^- $np_{x,y,z}$ orbitals.[30–33] *These orbitals differ little from the free* Hal^- *ones*. The difference is mainly due to polarization by the surrounding ions.[32] The binding energy of the valence-band electrons is essentially the electron affinity of a free Hal^- ion increased by the Madelung potential: the potential created by the rest of the ions in the crystal, treated as point charges, on a halogen site. Other contributions to the binding energy come from the valence band width (5 eV for LiF)[24,25] and from polarization (Mott-Littleton)[34] effects.

Consider electron capture by a projectile A^q, of charge q, scattered at the surface of an ionic crystal. The valence-band electrons being localized at the Hal^- crystal sites, one deals with *localized electron capture* whereby the projectile A^q undergoes a sequence of binary interactions with successive Hal^- crystal sites,

$$Hal^- + A^q \rightarrow Hal^0 + A^{q-1}. \tag{1}$$

In each of these binary interactions we have an *active site*: the site actually participating in the charge-transfer process. Owing to the flat and narrow valence bands of alkali-halide crystals, the hole mobility is low: i.e., the removal of an electron from a Hal^- site leaves the corresponding hole localized at that site[35] on the time scale of the collision. Other arguments supporting the idea of negligible hole diffusion during the collision event are given in Appendix A.

Figure 2 displays schematically the binary collision event Eq. (1). The active site is taken at the origin of a reference frame in which the **R** vector locates center *A*. Other ions of the crystal are *spectators* and will be considered as point charges.

A. Energy-level confluence

A key feature of the electron-transfer mechanism is the difference between the energies of the initial-like ($Hal^- + A^q$) and final-like ($Hal^0 + A^{q-1}$) states:

$$\Delta E(\mathbf{R}) = E(Hal^0 + A^{q-1}) - E(Hal^- + A^q). \tag{2}$$

For simplicity we will first neglect polarization effects, including image potentials. Exploiting the characteristics of alkali-halide surfaces dwelt on in the introductory part of this section, we have

$$E(Hal^- + A^q) = E_{Hal^-} + E_{A^q} + \sum_{i \neq j} \frac{q_i q_j}{|\mathbf{r}_i - \mathbf{r}_j|} - \sum_i \frac{q_i}{|\mathbf{r}_i|} + \sum_i \frac{q_i q}{|\mathbf{R} - \mathbf{r}_i|} - \frac{q}{R}. \tag{3}$$

In Eq. (3) the summations run over the point charges, i.e., *excluding the active site*. $R \equiv |\mathbf{R}|$; E_{Hal^-} and E_{A^q} are, respectively, the energies of the free Hal^- ion and A^q projectile; $q_i (= \pm 1)$ are the values of the point charges at the crystal sites. The third term is the interaction energy between the point charges. The fourth term is the interaction energy between the active site (having a charge -1) and all other sites of the crystal. The fifth term is the interaction energy between the projectile and the point charges. Finally, the last term is the interaction energy between the charge of the projectile and that of the active site. Similarly,

$$E(Hal^0 + A^{q-1}) = E_{Hal^0} + E_{A^{q-1}} + \sum_{i \neq j} \frac{q_i q_j}{|\mathbf{r}_i - \mathbf{r}_j|} + \sum_i \frac{q_i (q-1)}{|\mathbf{R} - \mathbf{r}_i|}, \tag{4}$$

Eq. (4) takes into account the fact that the removal of the electron from the active site leaves a null charge at this site. From Eqs. (3) and (4) we have

$$\Delta E(\mathbf{R}) = (E_{Hal^0} - E_{Hal^-}) - (E_{A^q} - E_{A^{q-1}}) + \left\{ \sum_i \frac{q_i}{|\mathbf{r}_i|} - \sum_i \frac{q_i}{|\mathbf{R} - \mathbf{r}_i|} \right\} + \frac{q}{R}. \tag{5}$$

The first and second terms in brackets give the binding energy of the electron to the *free* Hal^- ion ($\epsilon^{\text{binding}}_{Hal^-}$) and free A^{q-1} projectile ($\epsilon^{\text{binding}}_{A^{q-1}}$), respectively. The term in the curly brackets is the energy required to bring an electron initially located at $R = 0$ on the surface to the point $\mathbf{R}$ in the gas phase. This is the difference between the Madelung potentials created by the point charges at the Hal^- site [$E_{\text{Mad}}(0) \equiv E_{\text{Mad}}$] and at the point $\mathbf{R}$ [$E_{\text{Mad}}(\mathbf{R})$]. The last term is the energy required to neutralize the Hal^- ion in the field of the A^q projectile. Finally, Eq. (5) can be rewritten as

$$\Delta E(\mathbf{R}) = \Delta \epsilon^{\text{binding}} + E_{\text{Mad}} - E_{\text{Mad}}(\mathbf{R}) + \frac{q}{R}, \tag{6}$$

with

$$\Delta \epsilon^{\text{binding}} = \epsilon^{\text{binding}}_{Hal^-} - \epsilon^{\text{binding}}_{A^{q-1}}. \tag{6'}$$

Let us consider the case $R \gg a$, where a is the lattice constant. For a distant charge, a hole created on the neutral crystal by the removal of a negative charge at the active site is seen as a $+1$ charge. So, $E_{\text{Mad}}(\mathbf{R}) \sim 1/R$ and Eq. (6) transforms to

$$\text{for } R \gg a: \Delta E(\mathbf{R}) \sim \Delta \epsilon^{\text{binding}} + E_{\text{Mad}} + \frac{q-1}{R}. \tag{7}$$

Intuitively, the meaning of Eq. (7) is quite clear. Initially we had an electron at the Hal^- crystal site and the A^q projectile in front of the *neutral* crystal. So, except for polarization effects, the relevant energy is given by the energy of the mentioned electron: $E_{\text{Initial}} = -E_{\text{Mad}} - \epsilon^{\text{binding}}_{Hal^-}$. The final state corresponds to the electron located at the A^{q-1} projectile in presence of a hole (at the origin of coordinates) on the crystal; the latter is equivalent to a positive charge at $R = 0$. The corresponding energy is $E_{\text{Final}} = (q-1)/R - \epsilon^{\text{binding}}_{A^{q-1}}$. Equation (7) is just the $E_{\text{Final}} - E_{\text{Initial}}$ difference.

Let us illustrate our approach with two examples: (i) negative-ion formation via electron capture by a neutral projectile, $q = 0$, and (ii) neutralization of a singly charged positive ion, $q = +1$.

In case (i) Eq. (7) becomes

$$\Delta E(\mathbf{R}) \sim \Delta \epsilon^{\text{binding}} + E_{\text{Mad}} - \frac{1}{R}. \tag{8}$$

The attractive $-1/R$ term in Eq. (8) initiates the *confluence of the energy levels* of the initial-like and final-like states.

In case (ii) Eq. (7) becomes

$$\Delta E(\mathbf{R}) \sim \Delta \epsilon^{\text{binding}} + E_{\text{Mad}}. \tag{9}$$

Thus except for polarization effects, which are likely to be significant for large q, *no confluence of energy levels occurs for singly charged positive ions*.

Figure 3(a) displays $\Delta E(\mathbf{R})$ [Eq. (6)] for the case of F^- formation at a LiF(100) surface ($\Delta \epsilon^{\text{binding}} = 0$, $a = 7.592 a_0$). Figure 3(b) shows the same for Na^+ neutralization at the same surface ($\Delta \epsilon^{\text{binding}} = -1.689$ eV). The scattered particle is assumed to follow a straight-line trajectory in the $\langle 100 \rangle$ direction with a turning point located at $2.5 a_0$ above the F^- active site and forming an angle $\alpha = 2°$ with respect to the surface plane. Dashed lines represent the asymptotic behaviors given by Eqs. (8) and (9). Oscillations in the actual $\Delta E(\mathbf{R})$ curves correspond to the successive passage of the projectile over positive/negative crystal sites. One nicely sees in Fig. 3(a) how the energy levels come together thereby facilitating the electron transfer: close to the active site $\Delta E(\mathbf{R})$ is reduced to ~ 3 eV as compared to 12 eV at infinite separation. On the other hand, for the Na^+ neutralization the energy defect of the reaction remains large. This qualitatively explains the experimental results of Ref. 28, namely, in the range of projectile velocities where F atoms grazingly scattered from a LiF(100) surface are efficiently transformed into F^- ions Na^+ projectiles remain un-neutralized.

Note that in the case of F^+ and H^+ projectiles complete neutralization at the alkali-halide surfaces is observed.[36] This is so because the F and H energy levels lie in close resonance with the valence band of the target [Eq. (9)].

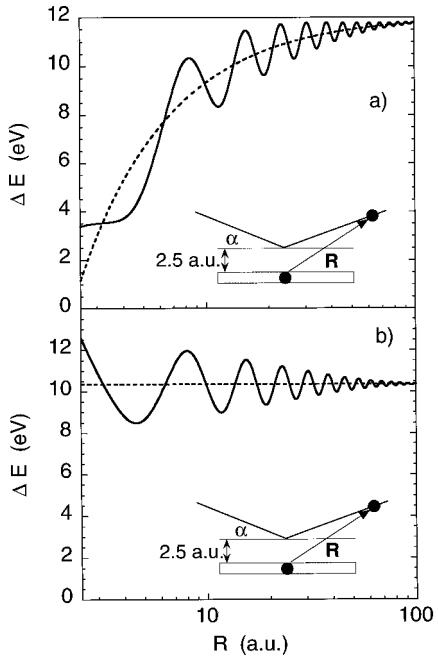

FIG. 3. Behavior of the energy difference ΔE between *final-like* and *initial-like* levels in A^q/LiF(100) *point-charge interactions* [reaction Eq. (1) of text]. The full and dotted lines are determined from Eqs. (6) and (7) respectively. Two cases are illustrated: (a) F^- ion formation from a neutral F projectile ($q=0$), and (b) neutralization of a positively charged Na^+ projectile ($q=+1$). ΔE is calculated as a function of the A^q-Hal distance R along the path showed schematically by the insets: specular reflexion with angle $\alpha=2°$ and turning point $R_{tp}=2.5a_0$. The oscillations are due to the passage of the produced F^- ion or reactant Na^+ ion above the successive ±1 point charges of the ionic crystal.

III. PARAMETER-FREE METHOD TO DESCRIBE ELECTRON CAPTURE BY F ATOMS GRAZINGLY SCATTERED FROM LiF(100) AND KI(100) SURFACES

As already stated in Sec. I, when treating negative-ion formation one should cope with two issues: (i) the *production* of negative ions by electron transfer from the target surface to the projectile, and (ii) the *survival* of the negative ion in front of the surface. The present work concerns the first part of the problem. The second part is still open though it was already discussed[9,13,37] that, owing to the large band gap in insulators, the destruction of negative ions, if at all possible, proceeds via kinematic effects, e.g., via kinematic tuning into resonance with conduction-band states. Therefore, we do not pretend to reproduce the complete shape of the parallel velocity dependence of the negative-ion production. Rather, we will concentrate on the low parallel velocity part of the experimental data, especially the parallel velocity thresholds and relative efficiency of the negative-ion production when changing the target or the scattering conditions (angle from the surface of the outgoing/incoming beam). Still, it will be seen below that the comparison of the computed and measured data enables one to draw some conclusions as to the electron loss (negative-ion destruction) process.

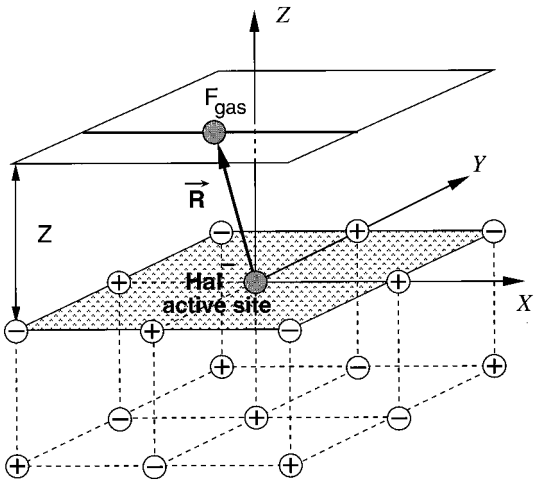

FIG. 4. Sketch of the considered binary interaction model. The shaded plane represents the portion on the last layer of the ionic surface surrounding a Hal^- active site (dark central circle). Circled $\pm$ symbols represents mere point charges. The straight line at a distance Z from the surface shows the trajectory of the impinging F_{gas} atom (dark upper circle) as it passes by. The **R** vector coincides with the z axis of a (direct Cartesian) reference frame accompanying the F_{gas} atom motion. The y axis of this rotating frame is defined to lie in the shaded plane. The x-axis definition ensues.

A. The model

We will consider the F projectile grazingly scattered along the ⟨100⟩ direction. Grazing scattering collisions are characterized by the small angle the trajectory has relative to the surface plane. At small projectile-surface separations where most of the charge transfer takes place, the projectile moves *almost parallel* to the surface.[38] One can then consider that *during its binary encounter with an active site* the particle moves along a trajectory parallel to the surface (Fig. 4).

To obtain the probability of the electron-transfer process [Eq. (1)] during the binary collision with an active site the following procedure is applied. First, one calculates electron-transfer probabilities $P(Y,Z)$ along a set of straight-line trajectories (Fig. 4) $\mathbf{R}(t)=(vt,Y,Z)$, where v is the projectile velocity. Then, the final transition probability $P^{site}(Z)$ in a binary collisions with an active site is obtained by averaging $P(Y,Z)$ over trajectories in the Y range $[-a/2,a/2]$ spanning a region of impact parameters per active site in the ⟨010⟩ direction:

$$P^{site}(Z)=\int_{-a/2}^{a/2} P(Y,Z)\,\frac{dY}{a}. \tag{10}$$

It is noteworthy that $P^{site}(Z)$ gives as well the probability of conversion into negative ions of a beam of neutral projectiles lying in an XY plane, at a distance Z from the surface, and traveling along the X direction (⟨100⟩), when crossing a row of surface atoms oriented along the Y direction (⟨010⟩) perpendicular to the beam. Indeed, if N_{proj} is the total number of projectiles and L is the size of the beam, then there are $(N_{proj}\,a)/L$ projectiles per active site and $[N_{proj}\,aP^{site}(Z)]/L$ negative ions formed per active site. Since there are L/a

active sites in the direction normal to the beam direction the total number of negative ions N^- is

$$N^- = \frac{N_{\rm proj}\, a P^{\rm site}(Z)}{L}\,\frac{L}{a} = N_{\rm proj} P^{\rm site}(Z). \tag{11}$$

Thus, the probability of conversion of neutral projectiles into negative ions when crossing a row of surface atoms is $N^-/N_{\rm proj} = P^{\rm site}(Z)$.

Projectiles scattered in the $\langle 100\rangle$ direction cross successive rows of surface atoms oriented in the $\langle 010\rangle$ direction at X_i points separated by $a/2$. So the final negative-ion yield can be evaluated as

$$P^{\rm total} = 1 - \prod_{i=1}^{N} \{1 - P^{\rm site}(Z_i)\}, \tag{12}$$

where $Z_i = Z(X_i)$ when $Z(X)$ is the trajectory of the scattered beam (see Sec. III D). Here we made the usual assumption for grazing scattering experiments[38] that the trajectory lies in the plane normal to the surface.

B. Description of the charge-transfer process

Here we deal with the calculation of the charge-transfer probability in the binary collision

$$F^0_{\rm gas} + {\rm Hal}^- \rightarrow F^-_{\rm gas} + {\rm Hal}^0, \tag{13}$$

where $F_{\rm gas}$ is the projectile moving along the $\mathbf{R}(t) = (vt, Y, Z)$ trajectory and Hal (F or I) is the active site on the alkali-halide [LiF(100) or Kl(100)] surface. Owing to the open p-shell structure of an actual halide atom, three levels emerge in each of the $F_{\rm gas}{}^0 + {\rm Hal}^-$ and $F_{\rm gas}{}^- + {\rm Hal}^0$ cases. These levels correspond to permutations of a hole among three $2p$-type (respectively, $5p$-type) orbitals in the case of F (respectively I). The wave function of the {projectile/active site} system can be expanded over a six-state *diabatic*[39] basis (to be defined below)

$$\Psi = \sum_{k=1}^{6} a_k \phi_k, \tag{14}$$

where

$$\phi_k \equiv \{\phi^{F^0_{\rm gas}}_{p_x}, \phi^{F^0_{\rm gas}}_{p_y}, \phi^{F^0_{\rm gas}}_{p_z}, \phi^{{\rm Hal}^0}_{p_x}, \phi^{{\rm Hal}^0}_{p_y}, \phi^{{\rm Hal}^0}_{p_z}\}. \tag{15}$$

$\phi^{F^0_{\rm gas}}_{p_\mu}$ basis states correspond to *initial-like* situations where the hole is located at the p_μ ($\mu = x$, y, or z) orbital of the $F_{\rm gas}$ projectile. $\phi^{{\rm Hal}^0}_{p_\mu}$ basis states correspond to *final-like* situations where the hole is located at the p_μ ($\mu = x$, y, or z) orbital of the Hal active site.

Our decision to single out the electron transfer in a binary collision introduces a *natural choice* of coordinate system, namely, the one whose z axis lies along the *molecular axis* $\mathbf{R}$, see Fig. 4. The other two axes are arbitrary and are chosen in such a way that the y axis lies in (or parallel to) the surface plane. The (x,y,z) reference frame is obtained by an orthogonal rotation matrix $\mathcal{R}$ from the fixed (X,Y,Z) one attached to the surface. The above indexing of the p_μ ($\mu = x$, y, or z) orbitals actually refers to the quantization of these orbitals in the *rotating* (x,y,z) reference frame.

The evolution of the wave function Ψ during the collision is given by the time-dependent Schrodinger equation,

$$i\,\frac{\partial \Psi}{\partial t} = H_{\rm electronic}\Psi, \tag{16}$$

where $H_{\rm electronic}$ is the Hamiltonian governing the motion of the considered electrons. The dependence on time of the problem arises through $\mathbf{R}(t)$. Assuming that the ϕ_k basis states in Eq. (14) are orthonormal, Eq. (16) becomes

$$i\,\frac{d\mathbf{A}}{dt} = \{\mathcal{H} - i\mathcal{T}\}\mathbf{A}. \tag{17}$$

$\mathbf{A}$ is the column vector of a_k coefficients in Eq. (14), $\mathcal{H}$ is the matrix of the $H_{\rm electronic}$ operator in the ϕ_k diabatic basis; therefore *it is not diagonal* in general. In particular, off-diagonal matrix elements of $\mathcal{H}$ between $\phi^{F^0_{\rm gas}}_{p_\mu}$ and $\phi^{{\rm Hal}^0}_{p_\mu}$ functions induce gas/surface electron transfer transitions. Off-diagonal matrix elements of $\mathcal{H}$ between $\phi^{F^0_{\rm gas}}_{p_\mu}$ and $\phi^{F^0_{\rm gas}}_{p_\nu}$ (or between $\phi^{{\rm Hal}^0}_{p_\mu}$ and $\phi^{{\rm Hal}^0}_{p_\nu}$) $\mu \neq \nu$ functions are related to polarization-type distortions and share the population of the p states around the $F_{\rm gas}$ (or the Hal) center. $\mathcal{T}$ is a *Coriolis-coupling* matrix that arises from the above-mentioned quantization of the basis states in the rotating reference frame (x,y,z): $\mathcal{T}_{kl} = -\mathcal{T}_{lk} = \langle \phi_k | \partial/\partial t | \phi_l \rangle$ (see end of Appendix B). Diabatic states are defined to have no other contribution to the $\langle \phi_k | \partial/\partial t | \phi_l \rangle$ matrix element than the one related to the just mentioned rotation; radial coupling matrix elements of the form $\langle \phi_k | \partial/\partial R | \phi_l \rangle$ that would arise from the variation of $|\mathbf{R}(t)|$ vanish or are negligible.[39]

C. Computation of the Hamiltonian matrix

The calculations described in this section concern the $\{F_{\rm gas} - e^- - {\rm Hal}\}$ binary system (Hal=F or I) in the field of a point charge alkali-halide surface (LiF or KI, respectively). The calculations involve 783 point charges organized in four parallel layers. This number was arrived at by requiring the calculated Madelung potential on the active site to be better than 5×10^{-4} eV in both cases. For the $\{F_{\rm gas} - e^- - {\rm F}\}$ system *all* the 19 electrons of the system were explicitely considered. For the $\{F_{\rm gas} - e^- - {\rm I}\}$ system we used an *ab initio* l-dependent pseudopotential[40] to represent the 46 inner-electrons of I. Except for the point charges, the computational work is very similar to that involved in atom-atom interactions and molecular structure calculations. Accordingly, it has been performed using a quantum chemistry computer code.[41]

For simplicity, all the reported calculations concern *single configuration state functions* (CSF) built from a single orthonormal set of (atomic or molecular) orbitals. The orbitals are determined from Hartree-Fock-Roothaan[42] self-consistent-field (SCF) schemes described below. This is achieved using expansions of the orbitals over contracted Gaussian basis sets: for F we used the double zeta basis of Ref. 43 while for I we used a $(3s3p)/[2s2p]$ contraction of the basis given in Ref. 44. Diffuse and polarization basis functions are added to

these bases to allow, respectively, for the description of the relevant negative ions and the distortion of the (neutral or negatively charged) atomic species in the field of the various point charges of the problem. The exponents of the additional basis functions are $\zeta_s(\mathrm{F})=0.11\,038$, $\zeta_p(\mathrm{F})=0.069$, $\zeta_d(\mathrm{F})=0.8$ and $\zeta_p(\mathrm{I})=0.03$, $\zeta_d(\mathrm{I})=0.29$.

1. Adiabatic calculations

Standard electronic structure calculations of molecular physics or quantum chemistry are oriented towards the determination of *adiabatic* states which are eigenstates of the electronic Hamiltonian $H_{\text{electronic}}$ for fixed positions of the nuclei. Our decision to treat the problem in terms of CSF's imposes that the adiabatic states correlated with the initial-like and final-like states of Eq. (13) have to be described by *creating a hole in the closed-shell configuration* of the $\{(\mathrm{F}-\mathrm{Hal})^{2-}$–point-charge surface$\}$ *reference system*. The relevant adiabatic states, noted η_i $(i=1,6)$ are obtained by permuting the hole among the corresponding six outer orbitals ω_i, ordered by increasing binding energy, in the reference closed-shell system. The requirement that

$$\langle \eta_i | H_{\text{electronic}} | \eta_j \rangle = 0 \quad (i \neq j) \tag{18}$$

entails that the orbitals constituting the adiabatic CSF's have to obey the condition

$$\langle \omega_i | F_{ij} | \omega_j \rangle = 0 \quad (i \neq j), \tag{19}$$

where

$$F_{ij} = h^C + \sum_{l \neq i,j}^{\mathcal{N}} \{2J_l - K_l\} + J_i + J_j . \tag{20}$$

h^C contains the kinetic energy of an electron and its interactions with all nuclei of the system (those of $\mathrm{F_{gas}}$ and Hal as well as all point charges describing the surface); $\mathcal{N}$ is the total number of occupied orbitals. J_l and K_l are the Coulomb and exchange operators,

$$J_l\, f(\mathbf{r}) = \int \mathbf{dr}'\, \frac{\omega_l^*(\mathbf{r}')\omega_l(\mathbf{r}')}{|\mathbf{r}-\mathbf{r}'|}\, f(\mathbf{r}),$$

$$K_l\, f(\mathbf{r}) = \int \mathbf{dr}'\, \frac{\omega_l^*(\mathbf{r}')f(\mathbf{r}')}{|\mathbf{r}-\mathbf{r}'|}\, \omega_l(\mathbf{r}). \tag{21}$$

Equations (18), (19) can actually be satisfied for *any pair* (i,j) of orbitals by performing, as has actually been done in the present work, an SCF calculation on the *closed-shell* $\{(\mathrm{F}-\mathrm{Hal})^{2-}$–point-charge surface$\}$ system. Though in this case the Fock-operator $F_{\text{closed-shell}}$ is different from the one in Eq. (20),

$$F_{\text{closed-shell}} = h^C + \sum_{l=1}^{\mathcal{N}} \{2J_l - K_l\}, \tag{22}$$

it is actually consistent with Eqs. (19), (20) owing to the property

$$J_l \omega_l = K_l \omega_l . \tag{23}$$

The above properties are extensions of the well-known Brillouin theorem.[45]

Our use of SCF eigenstates of $F_{\text{closed-shell}}$ [Eq. (22)]

$$F_{\text{closed-shell}} \omega_i = \epsilon_i \omega_i \tag{24}$$

entails that the energy difference of two CSF's, say η_i and η_j, is simply expressed in terms of the difference of the corresponding orbital energies:

$$\mathcal{E}_{\eta_j} - \mathcal{E}_{\eta_i} = \epsilon_i - \epsilon_j \tag{25}$$

(Koopman theorem).[42,46] Equation (25) comes in particularly handy since the dynamics of electron transitions actually depend on *energy differences* rather than absolute total energies; this turns out to be fortunate because the errors common to the considered CSF's (namely, correlation error and use of a unique set of orbitals) are canceled to a large extent.

To go further, and proceed to the determination of the diabatic states in Sec. III C 2, it is useful to note first that, at small R where the electron transfer is likely to take place, the ϵ_i energies (and consequently the $\mathcal{E}_{\eta_i}$ ones) are split into *two well separated sets of three levels*. This splitting actually reflects the effect of the electron transfer: the set I $(i=1,2,3)$ corresponds to antibonding orbitals while the set II $(i=4,5,6)$ corresponds to bonding orbitals. The resemblance of the present problem, in the mentioned conditions, with an atom-atom problem singles out the internuclear axis **R**, as already pointed out above. This makes it enticing to transform the ω_i orbitals in each set independently so that they have preferential orientations along one of the three axes x, y, or z. This is actually achieved using a slight adaptation of the procedure described in Appendix B. The transformed orbitals, in each set s $(=I,II)$, may then be viewed as (diatomiclike) π_x^s, π_y^s, and σ^s orbitals perturbed by the rest of the crystal. After this transformation, the diagonal Hamiltonian matrix $\boldsymbol{\mathcal{E}}$ in the adiabatic CSF basis [Eqs. (18), (24), (25)] becomes the block-diagonal $\tilde{\boldsymbol{\mathcal{E}}}$ matrix: $\tilde{\mathcal{E}}_{\mu\nu}^{I,II} \equiv 0$ $(\forall \mu,\nu)$. The nonzero $\tilde{\mathcal{E}}_{\mu\nu}^{s,s}$ $(\mu \neq \nu)$ matrix elements correspond to $\sigma^s - \pi_{x \text{ or } y}^s$ or $\pi_x^s - \pi_y^s$ couplings due to the crystal field which breaks the diatomic molecule symmetries in each set. The subscripts μ and ν have the same meaning here as those defined at the beginning of Sec. III B $(\mu\ [or\ \nu] = x,y,z)$.

From the preceding discussion one may interpret the diagonal energy differences between corresponding states in the two blocks,

$$\Delta_\mu = \tilde{\mathcal{E}}_{\mu\mu}^{I,I} - \tilde{\mathcal{E}}_{\mu\mu}^{II,II}, \tag{26}$$

as being directly related to the energy differences $\Delta E_\mu^{\text{Diabatic}} \equiv \mathcal{H}_{i\,i} - \mathcal{H}_{i+3\,i+3}$ and couplings $H_\mu^{\mathrm{F_{gas}^0 Hal^0}} \equiv \mathcal{H}_{i\,i+3} = \mathcal{H}_{i+3\,i}$ between electron transfer states in the diabatic basis, that is,

$$H_\mu^{\mathrm{F_{gas}^0 Hal^0}} = \frac{1}{2}\sqrt{\Delta_\mu^2 - (\Delta E_\mu^{\text{Diabatic}})^2}. \tag{27}$$

This amounts to make the approximation that the off-diagonal matrix elements of the diabatic $\boldsymbol{\mathcal{H}}$ matrix related to electron transfer preserve the symmetry label μ as would be the case for a pure $(\mathrm{F_{gas}}-\mathrm{Hal})^-$ system. We will see in Sec. III C 2 how we assess the quality of this approximation.

2. Diabatic states

The diabatic states for the present problem are obtained while keeping in mind the view, already put forward above, of an atom-atom system perturbed by the crystal field. Diabatic states for electron transfer processes are required to preserve the dominant characters the wave functions have in the initial and final stages of reactions of an Eq. (1) or (13) type. Stated differently, they should avoid mixings of these characters that may take place on the time scale of the collision. This is the way $\langle \phi_k | \partial/\partial R | \phi_l \rangle$ matrix elements are kept the smallest possible.[39] According to this prescription, a first step in our construction of diabatic states consists of hindering $F_{gas}-Hal$ two-center mixings related to electron transfer; the latters are taken care of in the dynamics [Eq. (17)] by off-diagonal elements of the $\boldsymbol{\mathcal{H}}$ matrix [Eq. (27)]. The mentioned constraint is imposed by preventing an electron that belongs to a given center to be describable in terms of wave functions centered around the other center and vice versa. To illustrate how this is achieved, in practice, let us consider two situations.

(a) *Initial-like wave functions: the* $\{F^0_{gas}-Hal^-$ *–point-charge surface*$\}$ *case*.

Clearly, if in this case one replaces the F^0_{gas} atom by a *null point charge* (noted ''0''), and describes explicitly the Hal^- ion embedded in the point-charge surface, there will be no tendency whatsoever of Hal^- wave functions to change in any way.

On another other hand, if one replaces the Hal^- ion by a mere -1 charge (noted ''$-$'') while describing explicitly the F^0_{gas} atom in front of the resulting point-charge surface, the F^0_{gas} p wave functions will change albeit by *mixing with wave functions belonging to the same center*. Here, distortion of the F^0_{gas} atomic functions by the crystal field has been allowed for but not electron transfer. In as much as the latter mixings can influence dynamically the electron-transfer process the diabatization procedure will have to go through a subsequent step described below.

At this stage of the procedure, the energy levels for the considered case have been obtained from two independent SCF calculations: one for an *actual* Hal^- ion embedded in the point-charge surface (''0''/Hal^-) and one for an *actual* $F_{gas}{}^0$ atom in the presence of the point-charge surface ($F_{gas}{}^0$/''$-$''). By *actual* $F_{gas}{}^0$ or Hal^- it is meant that this atom or ion is described *explicitly* as a CSF built from orbitals centered on it. For the $F_{gas}{}^0$/''$-$'' calculation we have made use of the properties of closed-shell CSF dwelt on in Sec. III C 1 [see Eqs. (22)–(25)], namely, $\mathcal{E}_i^{F^0_{gas}/''-''} = E^{F^-_{gas}/''-''} - \epsilon_i^{F^-_{gas}/''-''}$ $(i=1,2,3)$. We thereby get the initial-like energies,

$$\mathcal{E}_i^{(a)} = \mathcal{E}_i^{F^0_{gas}/''-''} + E^{''0''/Hal^-}. \tag{28}$$

(b) *Final-like wave functions: the* $\{F^-_{gas}-Hal^0$ *–point-charge surface*$\}$ *case*.

Following the same ideas as in the preceding paragraph, the energy levels for the considered case have been obtained from two independent SCF calculations: (i) one for an *actual* Hal^0 atom embedded in the point-charge surface and in the presence of a ''$-$'' charge in place of the F^-_{gas} ion (''$-$''/Hal^0), and (ii) one for an *actual* F^-_{gas} atom in the presence of the point-charge surface embedding a null charge at the Hal^0 site (F^-_{gas}/''0'').

Again, for the ''$-$''/Hal^0 calculation we have made use of the properties of closed-shell CSF presented Sec. III C 1, namely, $\mathcal{E}_i^{''-''/Hal^0} = E^{''-''/Hal^-} - \epsilon_i^{''-''/Hal^-}$ $(i=1,2,3)$. We thereby get the final-like energies,

$$\mathcal{E}_i^{(b)} = E^{F^-_{gas}/''0''} + \mathcal{E}_i^{''-''/Hal^0} - E^{''-''/''0''}. \tag{29}$$

The last term in Eq. (29) removes a Madelung contribution which would otherwise be counted twice $[E^{''-''/''0''}(\mathbf{R}) \equiv -E_{Mad}(\mathbf{R})]$. Here too, distortion of the Hal^0 atomic functions by the ''$-$'' charge at the F_{gas} center and the rest of the crystal field have been allowed for but not electron transfer.

Similarly to what has been done in Sec. III C 1, it is enticing to isolate in the results of the above cases (a) and (b) effects of the molecular ($F_{gas}-Hal$) axis, $\mathbf{R}$, from effects of the rest of the crystal. As mentioned there, this is done by transforming the open-shell orbitals or equivalently the corresponding hole states χ_i^α [$\alpha = F^0_{gas}$ or Hal^0 for cases (a) and (b), respectively], so that they have preferential orientations along the x, y, and z axes of the frame accompanying the motion of the $\mathbf{R}$ axis. Details of the procedure are given in Appendix B.

This procedure applied independently to the cases (a) and (b) transforms the diagonal Hamiltonian matrices $\boldsymbol{\mathcal{E}}^{(J)}$ $(J=a,b)$, Eqs. (28), (29), respectively, into $\tilde{\boldsymbol{\mathcal{E}}}^{(J)}$. Diagonal matrix elements $\tilde{\mathcal{E}}_{\mu\mu}^{(J)}$ of the latter matrices represent initial-like (respectively, final-like) energies modified by the privileged $F_{gas}-Hal$ axial distortions. These are the sought diabatic energy levels and thus the $\Delta E_\mu^{Diabatic}$ energy difference entering Eq. (27) reads

$$\Delta E_\mu^{Diabatic} = \tilde{\mathcal{E}}_{\mu\mu}^{(b)} - \tilde{\mathcal{E}}_{\mu\mu}^{(a)}. \tag{30}$$

Off-diagonal $\tilde{\mathcal{E}}_{\mu\nu}^{(J)}$ $(\mu \neq \nu)$ matrix elements correspond to couplings to atomic F^0_{gas} (or Hal^0) p-like states, in the molecular frame, due to the crystal field.

With the above, all ingredients are available to construct the diabatic $\boldsymbol{\mathcal{H}}$ matrix as

$$\boldsymbol{\mathcal{H}} = \begin{pmatrix} \boldsymbol{\mathcal{H}}^{F^0_{gas}F^0_{gas} \equiv \tilde{\boldsymbol{\mathcal{E}}}^{(a)}} & \boldsymbol{\mathcal{H}}^{F^0_{gas}Hal^0} \\ \boldsymbol{\mathcal{H}}^{Hal^0F^0_{gas}} & \boldsymbol{\mathcal{H}}^{Hal^0Hal^0 \equiv \tilde{\boldsymbol{\mathcal{E}}}^{(b)}} \end{pmatrix}, \tag{31}$$

where, using Eq. (27), we have

$$\boldsymbol{\mathcal{H}}^{F^0_{gas}Hal^0} = \begin{pmatrix} H_x^{F^0_{gas}Hal^0} & 0 & 0 \\ 0 & H_y^{F^0_{gas}Hal^0} & 0 \\ 0 & 0 & -H_z^{F^0_{gas}Hal^0} \end{pmatrix} = \boldsymbol{\mathcal{H}}^{Hal^0F^0_{gas}}. \tag{32}$$

The minus sign accompanying the $H_z^{F^0_{gas}Hal^0}$ coupling is related to the orientations of the p_z orbitals in the $\phi_{p_z}^{F^0_{gas}}$ and the

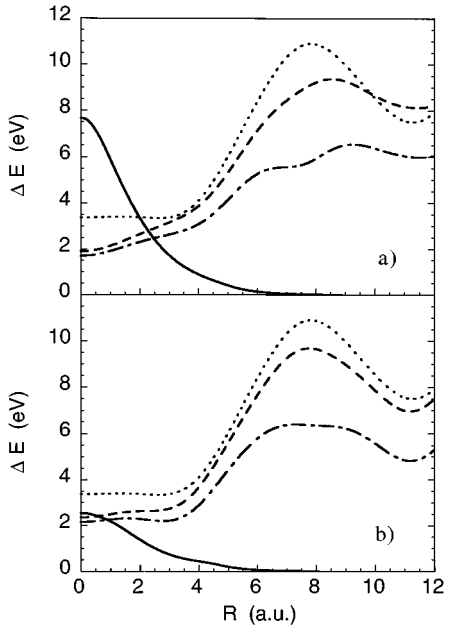

FIG. 5. Computed $\Delta E_{\mu}^{\text{Diabatic}}(R)$ diabatic energy difference (dashed line) and electron-transfer interaction $H_{\mu}^{F_{\text{gas}}^0 \text{Hal}^0}(R)$ (full line) in the considered binary interaction model for F/LiF(100). The results shown are obtained as a function of X along a straight-line trajectory $\mathbf{R}=(X,\ Y=0,\ Z=2.5a_0)$. Panels (a) and (b) show the results obtained for the $\mu=z$ and x states. The estimate $\Delta E^{\text{pc}}(R)$, from Eq. (6), for a mere point-charge surface is shown for comparison (dotted line). Beyond $R=12a_0$ the ΔE curves keep oscillating about $E_{\text{Mad}}-1/R$ as seen in Fig. 3(a), owing to the passage above consecutive ± 1 charges of the ionic crystal. Modifications of the $\Delta E_{\mu}^{\text{Diabatic}}(R)$ curves introduced by taking into account the Mott-Littleton contribution (E_{ML}) are shown by the dashed-dotted lines.

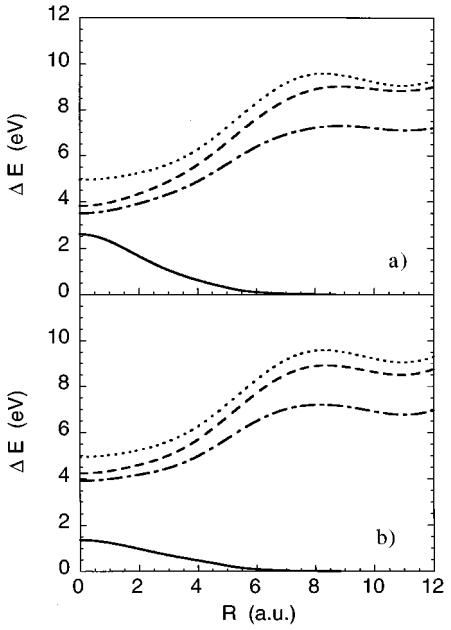

FIG. 6. Diabatic energy differences $\Delta E_{\mu}(R)$ and electron-transfer interaction $H_{\mu}^{F_{\text{gas}}^0 \text{Hal}^0}(R)$ for the F/LiF(100) case. Same caption and labeling as in Fig. 5, except that $Z_0=3.5a_0$.

$\phi_{p_z}^{\text{Hal}^0}$ states; when oriented in the same direction, as is the case here, the positive lobe of the p_z orbital of Hal^0 faces the negative p_z lobe on F_{gas}^0.

The consistency of the whole procedure ending up in Eq. (31) is finally checked by the diagonalization of the $\mathcal{H}$ matrix and the comparison of the resulting eigenvalues with the adiabatic ones of Sec. III C 1. The excellent comparison establishes the equivalence of the adiabatic and diabatic representations discussed above.

D. Calculation of the trajectory of the projectile

In the case of grazing scattering experiments (surface channeling conditions) the effective scattering potential seen by the approaching F atom is given by[38,47]

$$U(Z)=\left\langle \sum_{i_-} V_{\text{Hal}^-/\text{F}}(\mathbf{R}-\mathbf{r}_{i_-})+\sum_{j_+} V_{\text{Alk}^+/\text{F}}(\mathbf{R}-\mathbf{r}_{j_+}) \right\rangle_{X,Y}. \tag{33}$$

$V_{\text{Hal}^-/\text{F}}$ ($V_{\text{Alk}^+/\text{F}}$) is the binary interaction potential between the projectile and the halide (respectively, alkali) sites. In Eq. (33), the summation runs only over the surface sites with respective positions $\mathbf{r}_{i_-}$ ($\mathbf{r}_{j_+}$); the averaging is performed over all possible positions of the projectile in the (X,Y) plane parallel to the surface.

The binary interaction potentials in Eq. (33) have been determined from Hartree-Fock-Roothaan-SCF calculations similar to those described in the previous section. Likewise, the two relevant partners were treated explicitely while the rest of the crystal was modeled by point charges. In each case three binary potentials emerge. This corresponds to the permutation of the hole among the $2p_x$, $2p_y$, and $2p_z$ orbitals of the F_{gas}^0 atom. The binary potentials in Eq. (33) were taken to be the average of the latter three.

Knowing a potential $U(Z)$, the trajectory is determined by Newton's equations of motion. In particular, the turning point of the trajectory Z_{tp} is given by

$$U(Z_{\text{tp}})=E_{\perp}\equiv M\,\frac{v_{\perp}^2}{2}. \tag{34}$$

$v_{\perp}$ is the normal component of the velocity of the projectile and M its mass. It is noteworthy that, for the small values of the normal energy $E_{\perp}$ actually involved in grazing collision experiments, the potential $U(Z)$ calculated from Hartree-Fock-SCF binary interactions is less repulsive than the one which can be obtained from the universal Ziegler-Biersack-Littmark (ZBL) pair potentials.[48] This leads to smaller values of Z_{tp} with our choice of potential than those obtained from the ZBL pair interactions. As will be seen later on Z_{tp} is an important parameter controlling the negative-ion production. Our rejection of the ZBL-based potentials is due to their known failure to reproduce the experimental data for low $E_{\perp}$.[49–51]

IV. RESULTS

A. Hamiltonian matrix

Figures 5–10 show samples of results obtained from the diabatic $\mathcal{H}$ matrix computations of Sec. III C. Energy differ-

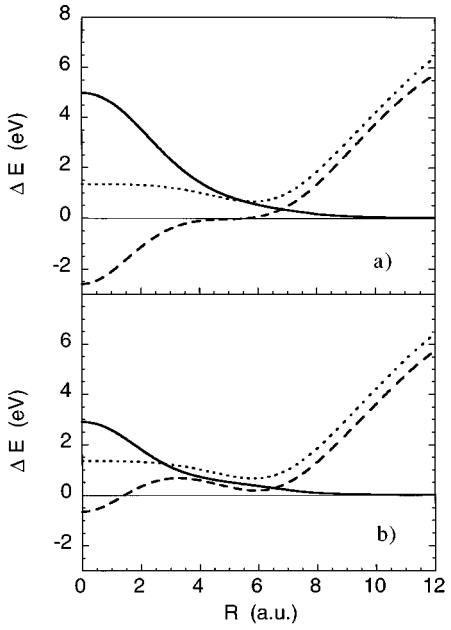

FIG. 7. Computed $\Delta E_{\mu}^{\text{Diabatic}}(R)$ diabatic energy difference (dashed line) and electron-transfer interaction $H_{\mu}^{\text{F}^0_{\text{gas}}\text{Hal}^0}(R)$ (full line) in the considered binary interaction model for F/KI(100). The results shown are obtained as a function of X along a straight-line trajectory $\mathbf{R}=(X,\ Y=0,\ Z=3.5a_0)$. Panels (a) and (b) show the results obtained for the $\mu=z$ and x states. The estimate $\Delta E^{\text{pc}}(R)$, from Eq. (6), for a mere point-charge surface is shown for comparison (dotted line). Beyond $R=12a_0$ the ΔE curves keep oscillating about $E_{\text{Mad}}-1/R$ as seen in Fig. 3(a) owing to the passage above consecutive ± 1 charges of the ionic crystal.

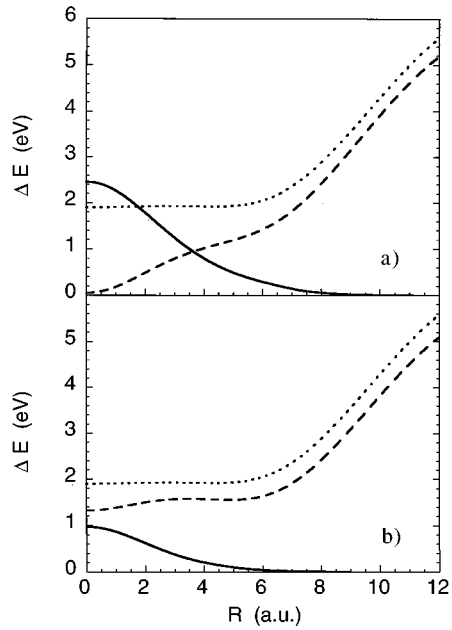

FIG. 8. Diabatic energy differences $\Delta E_{\mu}(R)$ and electron-transfer interaction $H_{\mu}^{\text{F}^0_{\text{gas}}\text{Hal}^0}(R)$ for the F/KI(100) case. Same caption and labeling as in Fig. 7 except that $Z=4.5a_0$.

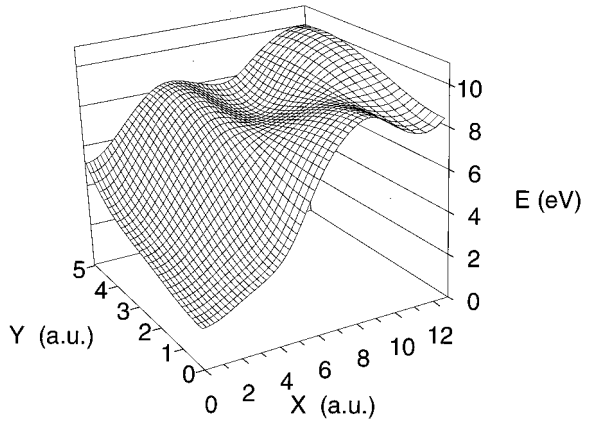

FIG. 9. Perspective view of the computed diabatic energy difference $\Delta E_z^{\text{Diabatic}}(\mathbf{R})$ for the F/LiF(100) case for trajectories of the F_{gas} projectile in the plane $Z=2.5a_0$. The confluence of energy levels for $X\rightarrow 0$ and $Y\rightarrow 0$ is clearly seen. The $Y=0$ cut of the displayed surface is the curve shown in Fig. 5(a). The undulations of the surface are due to the passage above consecutive ± 1 charges of the ionic crystal.

ences ($\Delta E_{\mu}^{\text{Diabatic}}$) and couplings ($H_{\mu}^{\text{F}^0_{\text{gas}}\text{Hal}^0}$) for electron transfer in the F/LiF(100) (Figs. 5, 6) and F/KI(100) (Figs. 7, 8) systems are displayed for two straight-line trajectories in the plane perpendicular to the surface and passing through the Hal active site at two characteristic distances Z from the surface plane. Comparison of corresponding panels (a) and (b) in these figures shows that among the p-type states, those having the largest $H^{\text{F}^0_{\text{gas}}\text{Hal}^0}$ couplings for comparable $\Delta E^{\text{Diabatic}}$ energy differences actually lie along $\mathbf{R}$ ($\phi_{p_z}^{\text{F}^0_{\text{gas}}}$ and $\phi_{p_z}^{\text{Hal}^0}$) as is the case in atom-atom systems. These σ-type

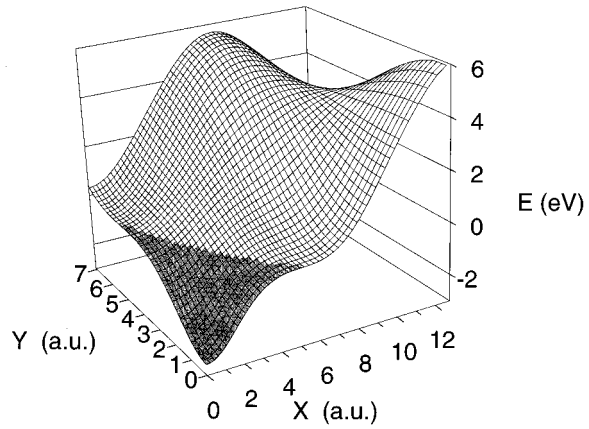

FIG. 10. Perspective view of the computed diabatic energy difference $\Delta E_z^{\text{Diabatic}}(\mathbf{R})$ for the F/KI(100) case for trajectories of the F_{gas} projectile in the plane $Z=3.5a_0$. As in Fig. 9 the confluence of energy levels is clearly seen. The shaded region of the surface corresponds to negative values of ΔE and draws attention to the existence of a potential surface crossing in this case. The $Y=0$ cut of the displayed surface is the curve shown in Fig. 7(a). The undulations of the surface are due to the passage above consecutive ± 1 charges of the ionic crystal.

states are expected to be the most efficient ones for the electron-transfer process and were called ''active'' states in Ref. 29.

A characteristics of the ($H_{\mu}^{F_{gas}^0 Hal^0}$) electron transfer coupling is its rapid decrease as R increases. This is well illustrated in each of the mentioned figures for fixed Z. The same tendency is seen when going from Fig. 5 to 6 (F/LiF(100)) and from Fig. 7 to 8 (F/KI(100)) where Z (and thus R) increases in otherwise the same conditions.

The overall appearance of the $\Delta E_z^{\text{Diabatic}}(\mathbf{R})$ energy differences along different straight-line trajectories $\mathbf{R}=(0\leqslant X\leqslant 12a_0, 0\leqslant Y\leqslant a/2, Z)$ are shown as perspective drawings in Figs. 9 and 10 for F/LiF(100) and F/KI(100), respectively. Note that due to the symmetry of the crystal, $\Delta E_{\mu}^{\text{Diabatic}}$ is a symmetric function of X and Y. The figures nicely illustrate the energy-level confluence whose mechanism was anticipated in Sec. II on the basis of interactions between mere point charges.

Figures 5–10 emphasize the *localized nature of the atom/ionic crystal surface* electron transfer. For F/LiF(100), the favorable region for electron transfer is likely to be localized around the locus of points where $H_{\mu}^{F_{gas}^0 Hal^0}\approx\Delta E_{\mu}^{\text{Diabatic}}/2$ as may be predicted from the Demkov[52]-Nikitin[53] near resonant electron-transfer model. For F/KI(100), $\Delta E_{\mu}^{\text{Diabatic}}(\mathbf{R})$ is seen to go through zero along certain trajectories (Figs. 7, 10). This feature indicates that a combination of Landau-Zener[54] curve-crossing mechanism and Demkov[52] near resonant mechanism will concur[53] in producing the F/KI(100) electron transfer. The presence of a potential-energy surface crossing in F/KI(100) lets one expect that electron transfer will be easier in this system than in F/LiF(100) where higher energies will be needed to overcome the resonance energy defect ($\approx 2-3$ eV, Figs. 5, 6).

Figures 5–8 show that the point-charge estimates of energy differences (ΔE^{pc}) for electron transfer, Eq. 6, account reasonably well for the results of the actual calculations. Yet one observes that, the larger R the better the agreement gets. This is understandable because the point-charge view holds only at large enough distances so that the detailed electronic structures of the partners does not matter anymore. This is particularly well illustrated by the F/KI(100) case where deviations between the $\Delta E_{\mu}^{\text{Diabatic}}$ calculations and the ΔE^{pc} point-charge estimates appear to be more pronounced than in the F/LiF(100) case. Indeed, the more diffuse I^- than F^- orbitals make the point-charge view breakdown at larger R in the former case than in the latter. A closer inspection of Figs. 5–8 actually reveals slight deviations between ΔE^{pc} and $\Delta E_{\mu}^{\text{Diabatic}}$ at distances as large as $R=12a_0$. In these figures the F_{gas} atom stays at a distance $Z\approx 2.5a_0-4.5a_0$ from the surface although its distance R to the active site increases. In these conditions, the ± 1 charges of the surface interact with the induced and/or permanent multipoles of the relevant atomic $F_{gas}^{0,-}$ species. Moreover the $Hal^{0,-}$ species at the active site is also polarized by the point charges on the surface. Contrary to the pure point-charge description, part of the latter interactions is taken into account in the calculated $\Delta E_{\mu}^{\text{Diabatic}}$ curves. The other part is taken provision of, in view of the dynamics calculation, in the off-diagonal $\tilde{\mathcal{E}}_{\mu\nu}^{(a)}$ matrix elements of Eq. (31).

The above discussion draws attention to the possibility that the part of the ionic crystal that is treated as ± 1 point charges in the actual calculations of Sec. III C could actually require polarization corrections. Indeed, electron capture by the F_{gas}^0 projectile from the Hal^- active site leads to a change of the electric field ''felt'' by the rest of the crystal. This is equivalent to the field created by an effective $\oplus-\ominus$ dipole whose $+1$ and -1 charges are located, respectively, at $\mathbf{R}_+=\mathbf{0}$ and $\mathbf{R}_-=\mathbf{R}$. This field should thereby interact with the dipoles it induces at the sites of the crystal so far treated as mere point charges. The corresponding (Mott-Littleton)[34] interaction energy can be expressed as follows;

$$E_{\text{ML}}=-\frac{\alpha_-}{2}\sum_{i_-}\left(\frac{\mathbf{r}_{i_-}-\mathbf{R}_+}{|\mathbf{r}_{i_-}-\mathbf{R}_+|^3}-\frac{\mathbf{r}_{i_-}-\mathbf{R}_-}{|\mathbf{r}_{i_-}-\mathbf{R}_-|^3}\right)^2. \quad (35)$$

The i_- index labels all the Hal^- sites except the active site. α_- is the polarizability of the Hal^- (F^-, I^-) sites of the ionic crystal, taken from Ref. 55. The terms in brackets give the electric field at the i_- sites due to the effective $\oplus-\ominus$ dipole. Equation (35) neglects contributions from the Alk^+ sites since the polarizability of Alk^+ ions is negligible compared to that of the Hal^- ions. Since the E_{ML} interaction energy arises in the final-like $\{F_{gas}^- - Hal^0 -$ point-charge surface$\}$ state the corresponding correction to the $\boldsymbol{\mathcal{E}}^{(b)}$ matrix [Eq. (31)] is

$$\mathcal{E}_{\mu\mu}^{(b)}\rightarrow\mathcal{E}_{\mu\mu}^{(b)}+E_{\text{ML}}. \quad (36)$$

Results for the $\Delta E_{\mu}^{\text{Diabatic}}(\mathbf{R})$ energy difference taking the E_{ML} energy correction for the F/LiF(100) case are displayed in Figs. 5, 6. In general, polarization of the point charges reduce $\Delta E_{\mu}^{\text{Diabatic}}(\mathbf{R})$ thereby facilitating electron transfer. The reduction is seen to be more important for $R\sim 8a_0$ corresponding to the passage of F_{gas}^- above an F^- crystal site in which conditions the polarization interaction maximizes.

Equation (35) actually relies on an asymptotic expression of the polarization interaction valid when the charges that induce the dipoles at the Hal^- crystal sites remain well outside the corresponding electron clouds. For the presently considered scattering conditions, the latter requirement applies to the case of F^- sites (in LiF) but not to that of I^- sites (in KI). This is due to the size of I^- ions which is much larger than that of F^-. Consequently, the E_{ML} correction has been taken into account in the F/LiF(100) calculations but not in the F/KI(100) ones. We believe that, owing to the comparatively smaller and even vanishing $\Delta E_{\mu}^{\text{Diabatic}}(\mathbf{R})$ energy difference in the latter case (Figs. 7, 8, 10), the omission of a proper E_{ML} correction is of little importance.

The smaller $\Delta E_{\mu}^{\text{Diabatic}}(\mathbf{R})$ energy differences in the F/KI(100) case as compared to the F/LiF(100) case actually arise from the larger lattice constant of the KI crystal ($a=13.34a_0$) than that of the LiF ($a=7.592a_0$) one. Indeed, as it follows from Eq. (6) for our case ($q=0$), $\Delta E(\mathbf{R})$ is governed by the difference of the Madelung potentials at the active site and at the position $\mathbf{R}$ of the projectile. One would thus expect that the smaller R is, compared to the characteristic size of the unit cell (a), the better equilibration of the Madelung energies can be achieved. This is why at the same Z distance smaller values of $\Delta E_{\mu}^{\text{Diabatic}}(\mathbf{R})$ are observed for the case of the KI(100) surface. In addition $\Delta\epsilon^{\text{binding}}=0$ for

the F/LiF(100) case while it is negative and amounts to -0.07 eV for the F/KI(100) case.

It should be mentioned at this point that the dynamics calculations, reported in Sec. IV B, as well as Figs. 5–10, are made consistent with the above ''exact'' values of $\Delta\epsilon^{\text{binding}}$. For the F/KI(100) case the so-called ''exact'' value of the $\epsilon_{I^-}^{\text{binding}}$ is obtained from exact data by removing the spin-orbit interaction in the neutral I atom according to

$$\epsilon_{I^-}^{\text{binding}}=\frac{2E_{I^0}(^2P_{3/2})+E_{I^0}(^2P_{1/2})}{3}-E_{I^-}. \tag{37}$$

Actually, in the F/LiF(100) case, the identical treatments of the Hal^- ($\equiv F^-$) and F_{gas}^- species leads automatically to the exact $\Delta\epsilon^{\text{binding}}=0$. However, this is not the case for F/KI(100) due to the different treatments of the F and I species (Sec. III). Application of the Koopman's theorem thus results in unbalanced errors in the two cases. This is corrected for to match the ''exact'' $\Delta\epsilon^{\text{binding}}$ by adding 1.4 eV throughout to the computed $\Delta E_{\mu}^{\text{Diabatic}}(\mathbf{R})$. To conclude this section we can say that, already on the basis of ''static'' results one can predict a more efficient F^- formation at a KI(100) surface compared to an LiF(100) surface.

B. Binary electron transfer

Given the $\mathcal{H}$ and $\mathcal{T}$ matrices Eq. (17) is solved along straight-line trajectories of the projectile $\mathbf{R}(t)=(vt,Y,Z)$. Three sets ($j=1,2,3$) of initial conditions were used for the amplitudes $\mathbf{A}^j(t\rightarrow-\infty)$,

$$a_k^j(t\rightarrow-\infty)=\delta_{kj}\quad(k=1,6). \tag{38}$$

These conditions correspond to permutations of the hole in the initial-like state among the p_x, p_y, and p_z orbitals of the approaching F_{gas}^0 projectile. The probability of negative-ion formation in the binary collision with an active site is obtained as the average over all initial conditions,

$$P(Y,Z)=\frac{1}{3}\sum_j \beta^j(Y,Z), \tag{39}$$

of the sum of electron-transfer probabilities $\beta^j(Y,Z)$ for each set of initial conditions,

$$\beta^j(Y,Z)=\sum_{k=4}^{6}|a_k^j(t\rightarrow+\infty)|^2. \tag{40}$$

Figures 11 and 12 display the Y and v dependences of computed $P(Y,Z)$ probabilities for given values of Z in the F/LiF(100) case. Owing to symmetry [$P(Y,Z)=P(-Y,Z)$], only the results for positive values of Y are presented. The figures show that for small velocities transitions occur only for trajectories passing close to the active site (small Y). This results from the fact that the energy difference between final-like and initial-like states $\Delta E_{\mu}^{\text{Diabatic}}$ is smallest for those trajectories (Fig. 9). The increase of $\Delta E_{\mu}^{\text{Diabatic}}$ on one hand and the decrease of the $\mathcal{H}^{F_{\text{gas}}^0\text{Hal}^0}$ interaction on the other hand strongly suppress transitions for large ''impact parameters'' Y. The increase of collision velocity is seen to be essential to activate the transitions for large Y.

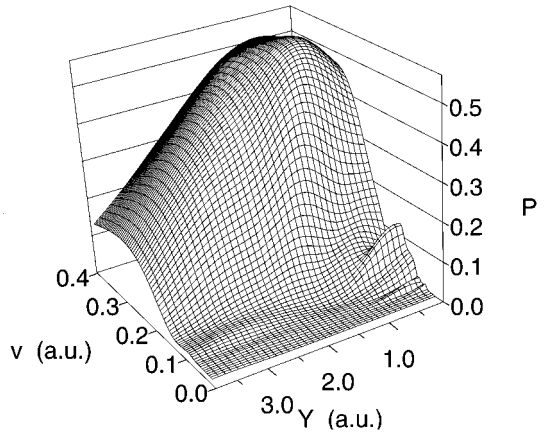

FIG. 11. Probability of electron transfer from an F^- active site at a LiF(100) surface to a collisional F atom in a single binary collision: $F_{\text{gas}}^0+F^-\rightarrow F_{\text{gas}}^-+F^0$. The calculation is done according to Eq. (39) of text for straight-line trajectories: $\mathbf{R}=(vt,Y,Z)$ in the plane lying at a distance $Z=2.5a_0$ from the surface. The figure displays, as a perspective view, the dependences of the probability $P(Y,Z=2.5a_0)$ upon parallel velocity v and ''impact parameter'' Y.

The structures of the charge-transfer probability $P(Y,Z)$ seen in Fig. 11 at low velocities are remnants of Stueckelberg oscillations[56] that are known to arise in atomic collision physics from the quantal interference of waves having traveled along different paths. Moreover, the velocity dependence of the computed electron-transfer probability can be well understood in terms of the Demkov-Nikitin exponential model of near resonant electronic transitions.[52,53]

The comparison of Figs. 11 and 12 shows that the increase of the Z distance from the surface leads to a substantial reduction of the electron-transfer probabilities and suppresses the low-velocity structures (Stueckelberg oscillations). As may be seen from Figs. 5 and 6 this is again a result of the concomitant increase of $\Delta E_{\mu}^{\text{Diabatic}}$ and decrease of the $\mathcal{H}^{F_{\text{gas}}^0\text{Hal}^0}$ interaction when the Z distance increases. It may thus be concluded that the region of small projectile

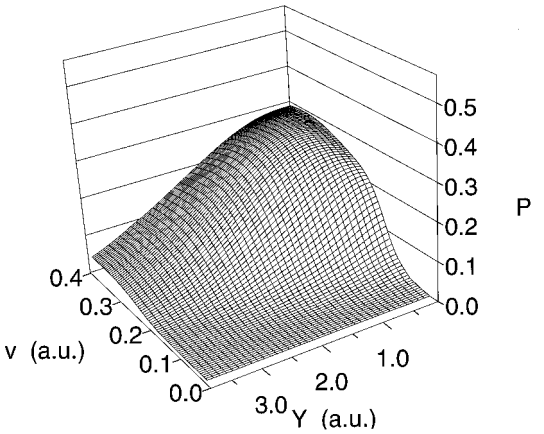

FIG. 12. Probability of electron transfer from an F^- active site at a LiF(100) surface to a collisional F atom in a single binary collision: $F_{\text{gas}}^0+F^-\rightarrow F_{\text{gas}}^-+F^0$. The calculation is done according to Eq. (39) of text. Same as Fig. 11 except that the Z distance from the surface is $Z=3.5a_0$.

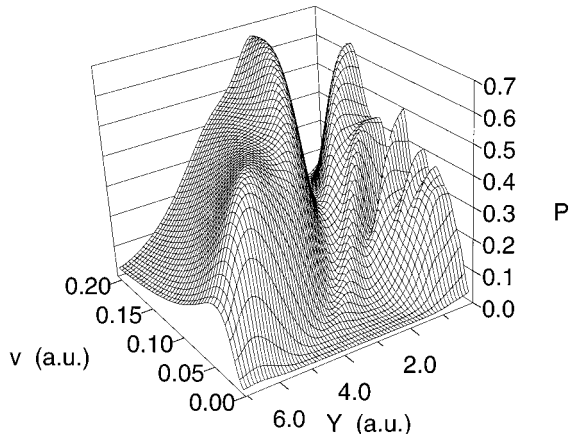

FIG. 13. Probability of electron transfer from an I^- active site at a KI(100) surface to a collisional F atom in a single binary collision: $F^0_{gas}+I^-\rightarrow F^-_{gas}+I^0$. The calculation is done according to Eq. (39) of text for straight-line trajectories: $\mathbf{R}=(vt,Y,Z)$ in the plane lying at a distance $Z=3.5a_0$ from the surface. The figure displays, as a perspective view, the dependences of the probability $P(Y,Z=2.5a_0)$ upon parallel velocity v and ''impact parameter'' Y.

surface separations (Z) will mostly contribute to the build up of negative-ion population.

Figures 13 and 14 display the Y and v dependences of computed $P(Y,Z)$ probabilities for given values of Z in the F/KI(100) case. Remarkable differences with respect to the F/LiF(100) case (Figs. 11, 12) are seen. This is particularly striking in the comparison of Figs. 12 and 13 which correspond to the same distance $(Z=3.5_0)$ from the surface: the transition probability is much higher and there is almost no parallel velocity threshold for negative-ion formation in the F/KI(100) case. Note that this is a relevant comparison since the important turning point region of the F projectile, as given by Eq. (34), is in the two cases: $2a_0\leqslant Z_{tp}\leqslant 4a_0$, for energies where fast onsets of negative-ion formation are observed.

Figure 13 shows rather complicate structures in the probability $P(Y,Z)$ as a function of the ''impact parameter'' Y

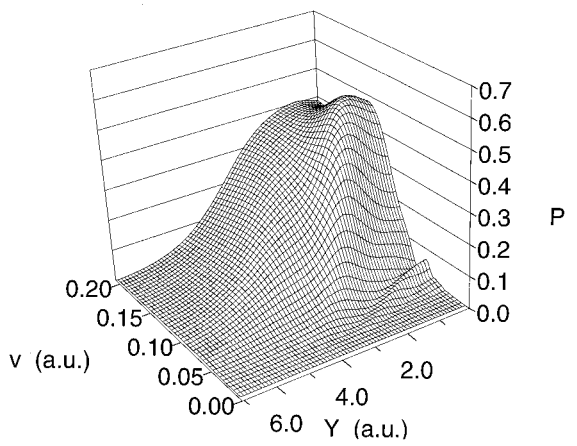

FIG. 14. Probability of electron transfer from an I^- active site at a KI(100) surface to a collisional F atom in a single binary collision: $F^0_{gas}+I^-\rightarrow F^-_{gas}+I^0$. Calculation is done according to Eq. (39) of text. Same as Fig. 13 except that the Z distance from the surface is $Z=4.5a_0$.

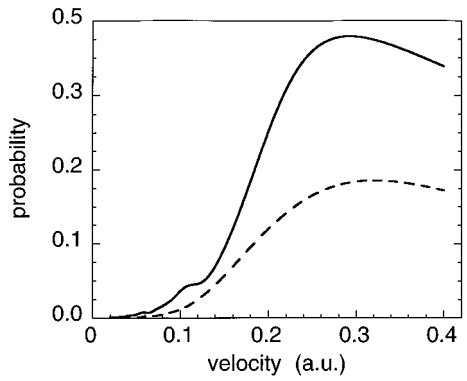

FIG. 15. Parallel velocity dependence of the probability of electron transfer $[P^{site}(Z)]$ from an F^- active site at a LiF(100) surface to a collisional F atom in a single binary collision: $F^0_{gas}+F^-\rightarrow F^-_{gas}+F^0$. $P^{site}(Z)$ is evaluated from Eq. (10) of text. Two representative values $Z=2.5a_0$ and $3.5a_0$ of the distance to the surface are displayed, solid and dashed lines, respectively.

and the parallel velocity v. The observed behavior is due to the existence of a crossing between the initial-like and final-like diabatic energy levels in this case (Figs. 7, 10). Two regions of ''impact parameters'' Y are seen to give rise to efficient electron transfer. These are actually related to the two transition mechanisms (Landau-Zener: curve-crossing[54] and Demkov: near resonant[52,53]) discussed in Sec. IV A. Efficient transitions at small ''impact parameter'' Y result from the curve-crossing mechanism while those occuring in the range $2a_0\leqslant Y\leqslant 4a_0$ are due to a near resonant mechanism with very small energy defect $(\Delta E_\mu^{\text{Diabatic}}\approx 0$, see Fig. 10). Further increase of Y suppresses the electron-transfer transitions as in the F/LiF(100) case.

The more efficient negative-ion formation in F/KI(100) as compared to F/LiF(100) clearly results from the smallness of the $\Delta E_\mu^{\text{Diabatic}}$ energy difference in F/KI(100). We have already mentioned in Sec. IV A that this feature is due to the lattice constant of the KI crystal which is almost twice as large as that of LiF. It turns out that the important distances for electron-transfer scale with the lattice constant. This is illustrated by Figs. 14 and 11 which, respectively, show that the $P(Y,Z=4.5a_0)$ results for F/KI(100) are very close to the $P(Y,Z=2.5a_0)$ results for F/LiF(100).

The changes observed for F/KI(100) by the increase of the Z distance to the surface when going from Fig. 13 to 14 are related to the disappearance of the curve crossing when going from Fig. 7 to 8. For $Z=4.5a_0$ (Fig. 14) the electron transfer thus proceeds via the Demkov near resonant mechanism[52,53] as is the case for F/LiF(100). This change of mechanism gives rise to a clear velocity threshold.

An important feature of the results presented in Figs. 11–14 is that, in the investigated velocity range and especially at the low velocities corresponding to the sharp onsets of negative-ion formation, the electron-transfer transitions are well localized in the ''impact-parameter'' region $-a/2\leqslant Y\leqslant a/2$. The half-lattice constant $a/2$ gives the distance between two neighboring Hal^- ions in the $\langle 010\rangle$ direction normal to the beam. The mentioned localization thus enables us to conclude that the electron-transfer regions correspond-

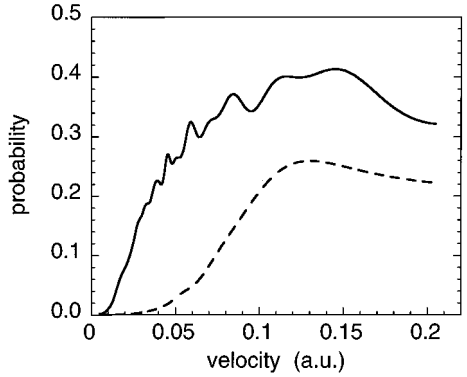

FIG. 16. Parallel velocity dependence of the probability of electron transfer ($P^{\text{site}}(Z)$) from an I^- active site at a KI(100) surface to a collisional F atom in a single binary collision: $F^0_{gas}+I^-\rightarrow F^-_{gas}+I^0$. The $P^{\text{site}}(Z)$ is evaluated from Eq. (10) of text. Two representative values $Z=3.5a_0$ and $4.5a_0$ of the distance to the surface are displayed, solid and dashed lines, respectively.

ing to the different Hal^- sites do not overlap. This gives *a posteriori* strong support to the binary-type model put forward in present work.

Results for the negative-ion formation probability per active site $P^{\text{site}}(Z)$ [Eq. (10)] are presented in Figs. 15 and 16 for the F/LiF(100) and F/KI(100), respectively. In both cases the increase of the Z distance to the surface is seen to reduce the electron-transfer probability and to move the velocity thresholds for negative-ion formation to larger values. Comparison of the two cases shows, as expected from the preceding discussions, that the onsets of negative-ion formation, for comparable Z distances, occur at smaller velocity values in F/KI(100) than in F/LiF(100).

C. Negative-ion conversion of neutrals

From the computed $P^{\text{site}}(Z)$ and the actual trajectories of the F projectile (Sec. III D), final negative-ion conversion probabilities of the F^0_{gas} atoms after grazing scattering from the LiF(100) and KI(100) surfaces are calculated from Eq. (12). The results are displayed in Figs. 17 and 18 along with experimental data of Ref. 13. As seen on the figures the results of the parameter-free study reproduce quite well the

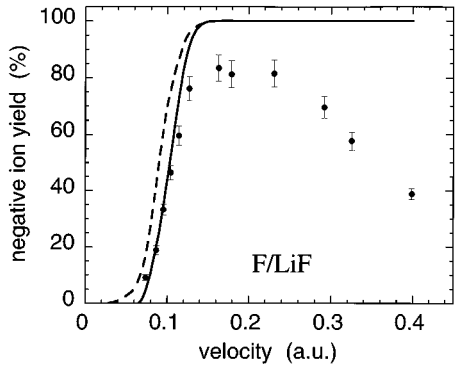

FIG. 17. Comparison of the negative-ion yield, versus parallel velocity, as measured for F/LiF(100) in Ref. 13 for an incidence angle $\alpha\approx 1°$ (data points) with present computations for two values of this angle: $\alpha=1°$ and 2.5°, solid and dashed lines, respectively.

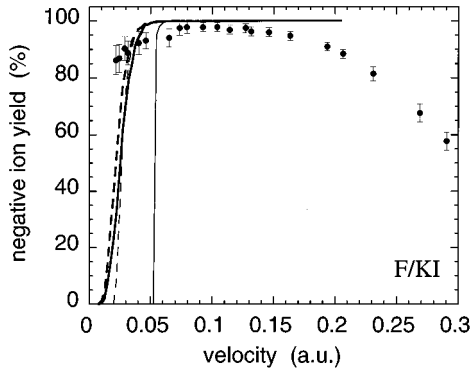

FIG. 18. Comparison of the negative-ion yield, versus parallel velocity, as measured for F/KI(100) in Ref. 13 for an incidence angle $\alpha\approx 1°$ (data points) with present computations for two values of this angle: $\alpha=1°$ and 2.5°, thick solid and dashed lines, respectively. The thin lines are the results of calculations disregarding image potential deceleration of the projectile in the outgoing path. This corresponds to a neutral atom trajectory. For $\alpha=1°$, a much higher parallel velocity threshold for negative-ion formation is found in this case. This feature is not connected to the properties of the electron transfer. It is due to the fact that the $E_\perp$ energy is so small that the projectile cannot get close enough to the surface.

low velocity part of the experimental data, including the velocity thresholds for the negative-ion formation. Note, that the fast increase of the negative-ion fraction after the threshold is not only due to the velocity dependence of the binary capture probability $P^{\text{site}}(Z)$ seen in Figs. 15 and 16 but also due to the increase of the number of binary collisions N with projectile velocity; as follows from Eq. (12), the negative-ion formation probability rapidly increases with N.

The theoretical results are presented for different angles α between the outgoing beam and the surface. The experimental data are to be compared with the calculation with $\alpha=1°$. The increase of the α angle shifts the velocity thresholds for negative-ion formation towards smaller v values, which corresponds to the experimental observations.[9,36,58] Indeed, the increase of the beam-surface angle leads to the decrease of the distance of the closest approach to the surface Z_{tp}. This in turn facilitates electron transfer in the low velocity region, as was demonstrated in the preceding sections.

It should be stressed that in the F/KI(100) case the experimentally measured negative-ion onsets occur for $E_\perp$ energies as low as 0.1 eV. With such energies the F^- ions cannot overcome the image potential barrier which is 0.6 eV (Refs. 26, 36, 59) and cannot leave the surface. Therefore the actual calculations have been performed with an ''effective'' angle γ obtained from the relation $E\gamma^2=E\alpha^2+0.6$, where E is the beam energy in eV. This relation expresses the fact that the $E_\perp$ energy near the surface is actually higher then the asymptotic one.[38,49,50] The effect of this correction is shown in Fig. 18. This sort of correction does not change the results for the F/LiF(100) case because of the much higher-energy thresholds for negative-ion formation.

For large velocities the theoretical results saturate, while the experimentally measured negative-ion fraction decreases. The failure of the presented approach to reproduce the experimental data at high velocities is due to the neglect of possible electron-loss processes leading to the destruction of

the negative ion. Owing to the large band gap of the alkali-halide surfaces, there are no electronic states of the surface in resonance with the affinity level of the negative ion [Fig. 1(b)]. Therefore, at small velocities electron losses are negligible.[28] The increase of the velocity opens possibilities for electron losses such as kinematic tuning into resonance with conduction-band states.[37,59] This explains why our approach reproduces well the experimental data only for small velocities.

Interestingly, the experimental data for F^- formation at a KI(100) surface do show a saturation of the negative-ion fraction as predicted by the theory. This is due to the very efficient electron capture by the projectile from the I^- active sites at low velocities, where practically no loss occurs. Comparing the experimental and theoretical data of Fig. 18, it is tempting to say that the threshold for the efficient electron losses leading to the F^- destruction corresponds to the velocity $v \approx 0.14$ a.u. F^- formation at an LiF(100) surface requires a comparatively much larger velocity so that the velocity regions for electron capture and electron loss start to overlap. This is the reason why no saturation of the F^- fraction is observed in this case (Fig. 17).

V. CONCLUSIONS

The evolution of the charge state of a projectile in grazing scattering from ionic (alkali-halide) crystal surfaces has been considered. The final charge fractions in the scattered beam are governed by (i) capture of the electron from the surface to the projectile; (ii) the survival of resulting species. Specific to insulators, the latter is particularly important owing to their large band gaps. Accordingly, and based on the localization of the valence-band electrons at the negatively charged (halogen) sites, a general approach to tackle the problem of *electron capture* in grazing scattering of projectiles from ionic-crystal surfaces has been proposed. It considers a build up of the charge state in the scattered beam as the result of a series of the binary electron-transfer processes between the projectile and negatively charged surface sites.

Based on this view a *parameter-free* study of F^- formation in grazing collisions of F atoms with LiF(100) and KI(100) surfaces has been performed. The corresponding calculations extend and improve those reported by us in Ref. 29. Our results demonstrate that electron transfer is indeed *localized* at the negatively charged F^- (I^-) sites at the surface. This justifies ''*a posteriori*'' the proposed approach for the negative-ion fraction build up.

The calculated F^- fractions correspond well to the experimental data in the *low-velocity region*. In particular, the experimentally observed velocity thresholds for negative-ion formation and the fast increase of the negative-ion fraction above threshold are reproduced. Moreover, the calculations reproduce the experimentally observed shifts of the negative-ion formation thresholds towards lower velocities with the increase of scattering angle. Pronounced differences in the efficiency of the F^- formation at KI(100) and LiF(100) surfaces are nicely explained.

As a final word of conclusion we may say that in order to reproduce the experimental data in the whole velocity range further work including the proposed approach for electron capture and incorporating dynamically assisted electron-loss process(es) is needed.

ACKNOWLEDGMENTS

We wish to acknowledge fruitful discussions with Professor J. P. Gauyacq (LCAM, Orsay) and Professor H. Winter (Humboldt University, Berlin).

APPENDIX A: ON HOLE DIFFUSION

The model considered in this paper is based on the idea that the hole created at the surface, as a result of electron transfer to the projectile, remains localized for the duration of the collision. This may be justified using energy considerations. Let us consider the case of Eq. (1) with $q=0$. The energy of the negative ion A^{-1} in front of the surface with a hole at the active site is given by Eq. (4) with $q=0$

$$E(\mathrm{Hal}^0+A^{q-1}) = E_{\mathrm{Hal}^0} + E_{A^{q-1}} + \sum_{i\neq j} \frac{q_i q_j}{|\mathbf{r}_i-\mathbf{r}_j|} - \sum_i \frac{q_i}{|\mathbf{R}-\mathbf{r}_i|}. \tag{A1}$$

Assume now that the hole jumped to a nearest Hal^- site at a position **b**. The energy $E'(\mathrm{Hal}^0+A^{q-1})$ of the new configuration is such that

$$E'(\mathrm{Hal}^0+A^{q-1}) - E(\mathrm{Hal}^0+A^{q-1}) = \frac{1}{R} - \frac{1}{|\mathbf{R}-\mathbf{b}|}, \tag{A2}$$

since the two situations differ only by the fact that one negative point charge on the surface was moved from the **b** position to **0**. Considering $\mathbf{R}=(0,0,2.5a_0)$ and $\mathbf{b}=(a/2,a/2,0)$, $a=7.592a_0$ (a is the lattice constant of the LiF crystal) the energy difference in Eq. (A2) amounts to 6.29 eV. This energy difference is quite large in comparison with the electron-transfer integral between the two sites. It is of the order of 0.56 eV as can be obtained from the SCF study (see also Figs. 5, 6). Based on these estimates it is quite likely that, during a binary collision, hole diffusion from an active site to a neighbor negative site should be suppressed.

APPENDIX B: TRANSFORMATION OF *p*-LIKE HAMILTONIAN MATRICES FROM THE FIXED FRAME TO THE MOLECULAR-FRAME REPRESENTATION

In this appendix we deal with the problem of isolating from p-like eigenvectors ψ_l ($l=1,3$) of Hamiltonian operators ($\hat{h}$) appearing in the treatment of reaction Eq. (13), effects of the molecular axis **R** from effects of the rest of the crystal. This is achieved hereunder by a transformation of the ψ_l's that aligns their dominant p component along one of the axes (x,y,z) of the reference frame attached to **R**. We have

$$\hat{h}\psi_l = d_l\psi_l, \tag{B1}$$

$$\hat{h}\underline{\psi} = \boldsymbol{\mathcal{D}}\underline{\psi}. \tag{B2}$$

In practice, the ψ_l's are written as expansions over an extended basis of Cartesian functions. From this expansion one may extract $\psi_{l(p)}$, the dominant p component of ψ_l,

$$\psi_{l(p)}=\sum_{\Lambda} C_{l\Lambda}P_{\Lambda}, \tag{B3}$$

$$\underline{\psi}_{(p)}=\mathcal{C}\underline{P}, \tag{B4}$$

the P_Λ's ($\Lambda=X,Y,Z$) are normalized Cartesian p functions quantized in the fixed reference frame attached to the surface (Fig. 4). One may rewrite Eqs. (B3), (B4) using corresponding p_μ functions ($\mu=x,y,z$) quantized in the molecular frame attached to **R**,

$$\underline{p}=\mathcal{R}\underline{P}. \tag{B5}$$

Since p functions transform as ordinary vectors under a rotation of the reference frame, $\mathcal{R}$ is the rotation matrix transforming the (X,Y,Z) reference frame into the (x,y,z) one (and $\mathcal{R}^T$ is its inverse). Hence

$$\underline{\psi}_{(p)}=\mathcal{G}\underline{p}, \tag{B6}$$

$$\mathcal{G}=\mathcal{C}\mathcal{R}^T. \tag{B7}$$

Because the $\psi_{l(p)}$ functions are neither orthogonal nor normalized $\mathcal{G}$ is not an orthogonal transformation,

$$\mathcal{G}\mathcal{G}^T=\mathcal{C}\mathcal{C}^T\equiv\mathcal{S}\neq\mathbb{1}. \tag{B8}$$

The $\mathcal{S}^{-1/2}$ orthogonalization method[57]

$$\underline{\psi}^{\perp}_{(p)}=\mathcal{S}^{-1/2}\underline{\psi}_{(p)}. \tag{B9}$$

actually provides the orthonormal vectors $\psi^{\perp}_{l(p)}$ that resemble the $\psi_{l(p)}$'s, and thus the ψ_l's, most. Thus from Eqs. (B6) and (B9) we obtain the transformation that allows us to bring the dominant p components of $\underline{\psi}$ in coincidence with $\underline{p}$; accordingly the Hamiltonian matrix [in Eq. (B2)] transforms as

$$\tilde{\mathcal{D}}=[\mathcal{S}^{-1/2}\mathcal{G}]^T\mathcal{D}[\mathcal{S}^{-1/2}\mathcal{G}]. \tag{B10}$$

The above transformation is determined by p_μ orbitals that are to be put in correspondence with the basis states specified in Eq. (15). Owing to Eq. (B5) it is easy to establish how the p_μ's vary in time along a trajectory $\mathbf{R}(t)=(vt,Y,Z)$. We have

$$\mathcal{R}=\frac{1}{R\rho}\begin{pmatrix} -Zvt & -ZY & \rho^2\dfrac{t}{|t|} \\ YR & -vtR & 0 \\ vt\rho & Y\rho & Z\rho \end{pmatrix}, \tag{B11}$$

where $R=|\mathbf{R}|$, $\rho=\sqrt{(vt)^2+Y^2}$. Accordingly, we have

$$\mathcal{U}_{\mu\nu}=\left\langle p_\mu\left|\frac{\partial}{\partial t}\right|p_\nu\right\rangle, \tag{B12}$$

$$\mathcal{U}=\mathcal{R}\frac{d\mathcal{R}^T}{dt}, \tag{B13}$$

and thus

$$\mathcal{U}=\frac{v}{(R\rho)^2}\begin{pmatrix} 0 & ZYR & -Z|vt|\rho \\ -ZYR & 0 & -Y(vt)^2 \\ Z|vt|\rho & Y(vt)^2 & 0 \end{pmatrix}. \tag{B14}$$

From this result the $\mathcal{T}$ matrix appearing in Eq. (17) is

$$\mathcal{T}=\begin{pmatrix} \mathcal{U} & 0 \\ 0 & \mathcal{U} \end{pmatrix}. \tag{B15}$$

[1] M. Szymonski, in *Desorption Induced by Electronic Transitions/DIET IV*, edited by G. Betz and P. Varga, Springer Series in Surface Science Vol. 19 (Springer, Berlin, 1990), p. 270.

[2] P. Varga and U. Diebold, in *Low Energy Ion-Surface Interactions*, edited by J. W. Rabalais (Wiley, New York, 1994), p. 355.

[3] P. Wurz, J. Sarnthein, W. Husinsky, G. Betz, P. Nordlander, and Y. Wang, Phys. Rev. B **43**, 6729 (1991).

[4] T. A. Green, J. M. Loubriel, P. M. Richards, N. H. Tolk, and R. F. Haglund, Jr., Phys. Rev. B **35**, 781 (1987).

[5] R. E. Walkup and Ph. Avouris, Phys. Rev. Lett. **56**, 524 (1986).

[6] D. Hasselkamp, in *Particle Induced Electron Emission II*, Springer Tracts in Modern Physics Vol. 123 (Springer, Berlin, 1992), p. 66.

[7] M. Vana, F. Aumayr, P. Varga, and H. P. Winter, Europhys. Lett. **29**, 55 (1995).

[8] R. Souda, K. Yamamoto, W. Hayami, T. Aizawa, and Y. Ishizawa, Phys. Rev. B **51**, 4463 (1995).

[9] C. Auth, A. G. Borisov, and H. Winter, Phys. Rev. Lett. **75**, 2292 (1995).

[10] J. Limburg, S. Schippers, R. Hoekstra, R. Morgenstern, H. Kurtz, F. Aumayr, and H. P. Winter, Phys. Rev. Lett. **75**, 217 (1995).

[11] F. Wiegershaus, S. Krischok, D. Ochs, W. Maus-Friedrichs, and V. Kempter, Surf. Sci. **345**, 91 (1996).

[12] S. Dieckhoff, H. Müller, W. Maus-Friedrichs, H. Brenten, and V. Kempter, Surf. Sci. **279**, 233 (1992).

[13] H. Winter, A. Mertens, C. Auth, and A. Borisov, Phys. Rev. A **54**, 2486 (1996).

[14] T. Hecht, C. Auth, A. Borisov, and H. Winter, Phys. Lett. A **220**, 102 (1996).

[15] F. W. Meyer, Q. Yan, P. Ziejlmans van Emmichoven, I. G. Hughes, and G. Spierings, Nucl. Instrum. Methods Phys. Res. B **125**, 138 (1997).

[16] M. Maazouz, L. Guillemot, S. Lacombe, and V. A. Esaulov, Phys. Rev. Lett. **77**, 4265 (1996).

[17] J. Los and J. J. C. Geerlings, Phys. Rep. **190**, 133 (1990).

[18] R. Brako and D. M. Newns, Rep. Prog. Phys. **52**, 655 (1989).

[19] D. Teillet-Billy and J. P. Gauyacq, Surf. Sci. **229**, 343 (1990).

[20] P. Nordlander, Phys. Rev. B **46**, 2584 (1992).

[21] J. N. M. van Wunnick, R. Brako, K. Makoshi, and D. M. Newns, Surf. Sci. **126**, 618 (1983).

[22] A. G. Borisov, D. Teillet-Billy, and J. P. Gauyacq, Phys. Rev. Lett. **68**, 2842 (1992).

[23] F. Wyputta, R. Zimny, and H. Winter, Nucl. Instrum. Methods Phys. Res. B **58**, 379 (1991).

[24] M. Piacentini and J. Anderegg, Solid State Commun. **38**, 191 (1981).

[25] D. A. Lapiano-Smith, E. A. Eklund, and F. J. Himpsel, Appl. Phys. Lett. **59**, 2174 (1991).
[26] C. Auth, T. Hecht, T. Igel, and H. Winter, Phys. Rev. Lett. **74**, 5244 (1995).
[27] L. Hägg, C. O. Reinhold, and J. Burgdörfer, Nucl. Instrum. Methods Phys. Res. B **125**, 133 (1997).
[28] A. Mertens, C. Auth, H. Winter, and A. Borisov, Phys. Rev. A **55**, R846 (1997).
[29] A. G. Borisov, V. Sidis, and H. Winter, Phys. Rev. Lett. **77**, 1893 (1996).
[30] A. B. Kunz, Phys. Rev. B **12**, 5890 (1975).
[31] A. Zunger and A. J. Freeman, Phys. Rev. B **16**, 2901 (1977).
[32] H. Tatewaki and E. Miyoshi, Surf. Sci. **327**, 129 (1995).
[33] G. K. Wertheim, J. E. Rowe, D. N. E. Buchanan, and P. H. Citrin, Phys. Rev. B **51**, 13 675 (1995).
[34] N. F. Mott and M. J. Littleton, Trans. Faraday Soc. **34**, 485 (1938).
[35] G. D. Mahan, Phys. Rev. B **21**, 4791 (1980).
[36] C. Auth, *Wechsclwirkung von Atomen und Ionen mit Metall- und Isolatoroberflachen bei der Streifenden Streung* (Shaker Verlag, Aachen, 1996).
[37] N. Lorente, J. Merino, F. Flores, and M. Yu. Gusev, Nucl. Instrum. Methods Phys. Res. B **125**, 277 (1997).
[38] H. Winter, J. Phys.: Condens. Matter **8**, 10 149 (1996).
[39] V. Sidis, Adv. Chem. Phys. **82**, 135 (1992).
[40] L. R. Kahn, P. Baybutt, and D. G. Truhlar, J. Chem. Phys. **65**, 3826 (1976). See also Ref. 44.
[41] M. Dupuis, J. D. Watts, H. O. Villar, and G. J. B. Hurst, Comput. Phys. Commun. **52**, 415 (1989).
[42] C. C. J. Roothaan, Rev. Mod. Phys. **23**, 69 (1951).
[43] R. Poirier, R. Kari, and I. G. Csizmadia, *Handbook of Gaussian Basis Sets*, Physical Sciences Data Vol. 24 (Elsevier, New York, 1985).
[44] W. R. Wadt and P. J. Hay, J. Chem. Phys. **82**, 284 (1985).
[45] See, e.g., R. McWeeny and B. T. Sutcliffe, *Methods of Molecular Quantum Mechanics* (Academic, London, 1989).
[46] T. Koopmans, Physica's Grav. **1**, 104 (1933).
[47] D. S. Gemmell, Rev. Mod. Phys. **46**, 129 (1974).
[48] J. F. Ziegler, J. P. Biersack, and U. Littmark, *The Stopping and Range of Ions in Solids* (Pergamon, New York, 1985).
[49] D. M. Goodstein, R. L. McEachern, and B. H. Cooper, Phys. Rev. B **39**, 13 129 (1989).
[50] C. A. DiRubio, R. L. McEachern, J. G. McLean, and B. H. Cooper, Phys. Rev. B **54**, 8862 (1996).
[51] R. Pfandzelter, F. Stölzle, H. Sakai, and Y. H. Ohtsuki, Nucl. Instrum. Methods Phys. Res. B **83**, 469 (1993).
[52] Yu. N. Demkov, Sov. Phys. JETP **18**, 138 (1964).
[53] E. E. Nikitin, Discuss. Faraday Soc. **33**, 14 (1962); E. E. Nikitin, Adv. Quantum Chem. **5**, 33 (1970); E. E. Nikitin and S. Ya Umanski, *Theory of Slow Atomic Collisions*, Springer Series in Chemical Physics Vol. 30 (Springer-Verlag, Berlin, 1984).
[54] L. D. Landau, Phys. Z. Sowjetunion **2**, 464 (1932); C. Zener, Proc. R. Soc. London, Ser. A **137**, 696 (1932).
[55] J. R. Tessman and A. H. Kahn, Phys. Rev. **92**, 890 (1953).
[56] E. C. G. Stueckelberg, Helv. Phys. Acta **5**, 369 (1932).
[57] P. O. Löwdin, Adv. Quantum Chem. **5**, 185 (1970).
[58] H. Winter (private communications).
[59] H. Winter, C. Auth, and A. G. Borisov, Nucl. Instrum. Methods Phys. Res. B **115**, 133 (1996).